

Numerical study on gas–liquid nano-flows with pseudo-particle modeling and soft-particle molecular dynamics simulation

Feiguo Chen · Wei Ge · Limin Wang ·
Jinghai Li

Received: 9 November 2007 / Accepted: 7 March 2008 / Published online: 27 March 2008
© Springer-Verlag 2008

Abstract We couple pseudo-particle modeling (PPM, Ge and Li in Chem Eng Sci 58(8):1565–1585, 2003), a variant of hard-particle molecular dynamics, with standard soft-particle molecular dynamics (MD) to study an idealized gas–liquid flow in nano-channels. The coupling helps to keep sharp contrast between gas and liquid behaviors and the simulations conducted provide a reference frame for exploring more complex and realistic gas–liquid nano-flows. The qualitative nature and general flow patterns of the flow under such extreme conditions are found to be consistent with its macro-scale counterpart.

Keywords Gas–liquid two-phase flow · Nano-flow · Molecular dynamics · Pseudo-particle modeling

List of symbols

Ca	capillary number (–)
F, F, f	force (kg m s^{-2})
g	gravitational acceleration (m s^{-2})
H	height (m)
k_B	Boltzmann constant ($k_B = 1.38 \times 10^{-23} \text{ kg m}^2 \text{ s}^{-2} \text{ K}^{-1}$)
L_s	slip length (m)
m	mass (kg)
N	number (–)
n	number density (m^{-dim^*})
P	position (m)

P	pressure ($\text{kg m}^{2-\text{dim}} \text{ s}^{-2}$)
R	radius (m)
Re	Reynolds number (–)
r	distance (m)
s	displacement (m)
T	temperature (K)
t	time (s)
U, u, V, v	velocity (m s^{-1})
W	width (m)
w	mass fraction (–)
x	coordinate, molar fraction (–)
y	coordinate
Z	compressibility factor (–)

Subscripts

b	bubble
c	critical
ct	control temperature
D	drag
g	gas phase
l	liquid phase
m	mean value
s	surface, interfacial
w	wall

Greek letters

Δ	increment
δ	Kronecker delta function
$\varepsilon, \phi, \Psi_s, \zeta$	potential energy ($\text{kg m}^2 \text{ s}^{-2}$)
η	packing fraction (–)
ρ	mass density ($\text{kg m}^{-\text{dim}}$)
μ	dynamic viscosity ($\text{kg m}^{2-\text{dim}} \text{ s}^{-1}$)
ν	kinematic viscosity ($\text{m}^2 \text{ s}^{-1}$)
τ	shear stress ($\text{kg m}^{2-\text{dim}} \text{ s}^{-2}$)
τ_l	characteristic time of liquid molecule (s)

F. Chen · W. Ge (✉) · L. Wang · J. Li
Institute of Process Engineering, Chinese Academy of Sciences,
Beijing 100190, People's Republic of China
e-mail: wge@home.ipe.ac.cn

F. Chen · L. Wang
Graduate University of Chinese Academy of Sciences,
Beijing 100039, People's Republic of China

*dim = 2 the dimensionality of the simulated system,
or 3 for the two- or three-dimensional system

1 Introduction

Micro- and nano-flows are receiving increasing attentions with the development of micro-electrical mechanical systems (Ho and Tai 1998; Jensen 1999; Stone et al. 2004), micro-chemical engineering (Jensen 1999; Gogotsi et al. 2002). Simulations of single-phase micro-/nano-flows have been widely reported (e.g., Hannon et al. 1986; Sun and Ebner 1992) and their theoretical foundations are relatively well established, such as their kinetic theory (Gad-el-Hak 2005) and slip boundary conditions (Thompson and Troia 1997; Gad-el-Hak 1999; Ellisab and Thompson 2004). As to multi-phase/component flows, although MD simulations at the interfaces (contact lines) between different fluids, fully immiscible (Kotsalis et al. 2004), with phase transitions (Peters and Eggebrecht 1995), or with sharp concentration gradients (Denniston and Robbins 2001), have been reported, the coverage to their bulk flow fields remains sparsely (We note that vacuum bubbles in liquids have been simulated (Matsumoto and Matsuura 2004), but the gas phase is completely ignored]. This constitutes one of the motivations for our work. However, the reason for us to focus more specifically on gas–liquid flows, which are encountered in, e.g., absorption and condensation process of vapors in micro-channels (Gad-el-Hak 1999), fuel cells (Chobana et al. 2004) and carbon nano-tubes (Yarin et al. 2005) is based on the following perception.

It is true that, at macro-scales, the flow behaviors and transport properties of both gases and liquids are described by the same set of continuum laws, although their quantitative differences are remarkable. But at nano-scales, flow behaviors are tightly coupled with statistical fluctuations and thermal movements of the molecules without clear scale separation, which means that the material properties used in continuum descriptions are not well defined and the details of molecular interactions may affect flow behaviors and transport processes in a complicated way.

Therefore, it becomes necessary to keep the specific modes of interactions for gases and liquids. Typically, gas molecules are reasonably assumed to be in free flight for most of the time, diverted by transient inter-collisions occasionally. Liquid molecules are, on the contrary, in strong and constant interactions with their neighbors, which prohibit an integral treatment of the interactions as binary collisions. To keep these characteristics, the gas phase is simulated by a hard-particle variant of MD called pseudo-particle modeling, PPM (Ge 1998; Ge and Li 2003; Ge et al. 2005), while the liquid phase is simulated by soft-

particle type MD with the traditional Lennard–Jones (LJ) potentials. In contrast, soft-particle models have been used for both fluids in the simulations cited earlier, with no sharp difference in the interactions among the molecules of different fluids. Alternatively, we may use soft potentials with very compact support; however, it will be computationally expensive and inaccurate, which proves to be unnecessary.

With this treatment, the physical picture of the nano-flows that we will explore is somewhat different from the two-fluid flows previously studied by Sushko and Cieplak (2001) who used LJ type interactions for both fluids. One may argue that, any gaseous structures at nano-scales, such as bubbles, cannot withstand the extremely high surface tension of surrounding liquid phase, and will be either dissolved or crushed to high densities where gases behave like liquids (say, in a supercritical state). However, this may, on the other hand, demonstrate the unique role of our model for theoretical studies. In fact, the purpose of this study is to understand how scale effect alone affects the flow behavior of a gas–liquid mixture in channels, so that the unique effects of other more complicated factors can be identified more easily in future studies with more realistic models. For this purpose, we have deliberately set the simulation parameters to artificial values, which can prevent the interpenetration of the two phases, so that the effect of phase-equilibrium can be excluded. Anyway, the primary effect we want to study, i.e., the scale effect, is reasonably inherent in our model, and except for that, the model keeps the properties of gases at macro-scales fairly well. Therefore, although our model may be inconsistent with the realities at nano-scales in some aspects, it can provide an idealized and simplified model of real systems, which is inaccessible in the physical world, to serve as a reference frame in calibrating the effect of other features in more realistic and complicated models.

The flow behaviors of a gas–liquid mixture in two-dimensional channels are studied in this work, which show both similarities and uniqueness in comparison with their macro-scale counterparts. The simulation details and analysis on the results are presented in the following sections.

2 Simulation approaches

The simulation approaches employed in this work are basically of the MD catalogue. The flows are driven by applying external forces. The time-integration of the equation of motion for each particle is carried out along with the statistics and analysis on the evolutionary flow patterns.

2.1 Interactions

The liquid phase is considered as a collection of circular molecules for the two-dimensional simulations carried out in this work. Newton’s second law is considered valid to describe the motion of these particles, which takes the form of

$$m \frac{d\mathbf{v}_i}{dt} = \sum_{i \neq j} \mathbf{F}_{ij} + \mathbf{F}_e \tag{1}$$

where \mathbf{F}_{ij} is the force between particles i and j , and \mathbf{F}_e is the external force such as gravity. A commonly used potential for simple fluids, the truncated and shifted Lennard–Jones (LJ) potential, is adopted to calculate the force between these particles. That is,

$$\phi(r_{ij}) = \begin{cases} 4\epsilon \left[\left(\frac{\sigma}{r}\right)^{12} - \left(\frac{\sigma}{r}\right)^6 + \left(\frac{\sigma}{r_c}\right)^6 - \left(\frac{\sigma}{r_c}\right)^{12} \right] & r_{ij} = |\mathbf{r}_i - \mathbf{r}_j| \leq r_c \\ 0 & r_{ij} > r_c \end{cases} \tag{2}$$

where σ is the characteristic length of the interaction that is usually taken as the particle diameter, ϵ is the energy parameter characterizing the interaction strength and r_c stands for the cutoff distance. The resulting force is then

$$\mathbf{F}_{ij} = -\nabla\phi(r_{ij}) = \left(\frac{48\epsilon}{\sigma^2}\right) \left[\left(\frac{\sigma}{r_{ij}}\right)^{14} - \frac{1}{2} \left(\frac{\sigma}{r_{ij}}\right)^8 \right] \mathbf{r}_{ij} \tag{3}$$

The state of the LJ fluid is dependent on the temperature and density of these particles, which is chosen to be liquid in this work.

For the gas phase, its state can be ensured by hard-particle (disk in 2D space) models of fluids when the packing fraction (η) of the particles is not too high (otherwise they solidify), since attractive interaction is absent. An advantage of hard-particle models is the ability to keep exact energy conservation (to machine accuracy). However, event-driven algorithms (Marin et al. 1993) are required by these models, which are not flexible in complicated situations, inefficient for large-scale simulations and not convenient for analyzing the results, ascribing to their inherently asynchronous and sequential nature.

The gas phase in this work is simulated with PPM which justifies the application of time-driven algorithms, as used in soft-particle models, to a hard-particle model with variable particle size, in which the so-called pseudo-particles (PPs) undergo free flights and transient collisions at synchronized paces for overlapping particles. That is, if the distance between two PPs, $|\mathbf{P}_1 - \mathbf{P}_2|$, is less than the sum of their radius (σ_g), and the inner product of $\mathbf{P}_1 - \mathbf{P}_2$ and $\mathbf{v}_1 - \mathbf{v}_2$ is negative, they will collide as two rigid and smooth spheres (or disks in 2D), resulting

$$\mathbf{v}_1 = \mathbf{v}_{10} - \frac{(1 + e)m_2 (\mathbf{v}_{10} - \mathbf{v}_{20}) \cdot (\mathbf{P}_1 - \mathbf{P}_2)}{m_1 + m_2 |\mathbf{P}_1 - \mathbf{P}_2|^2} \cdot (\mathbf{P}_1 - \mathbf{P}_2) \tag{4}$$

where \mathbf{v}_1 , \mathbf{v}_2 and \mathbf{v}_{10} , \mathbf{v}_{20} are the post- and pre-collision velocities for each particle, respectively, m_1 and m_2 are the constant mass of PPs, and e is the restitution coefficient which is normally set to unity for PPs. In the next time step, the particles move to new positions with their new velocities, and so on. Collisions are processed in a predefined sequence that can guarantee spatial homogeneity and isotropy.

The PPM method has been validated for the simulation of gas flow, e.g., duct flow, flow around a single cylinder, etc., and gas–solid flow, e.g., fluidization, as we have previously reported (Ge 1998; Ge and Li 2003; Ge et al. 2005; Wang et al. 2007), while the validity of the LJ model as a general model for simulating the flow of liquids has long been demonstrated in many publications.

For convenience, reduced values are used in the following simulations. For the PPs of the gas phase, $\sigma_g = 0.5$ and $m_g = 0.1$ are selected and the corresponding parameters for the LJ potential of the liquid phase are $\sigma_l = 1$, $\epsilon_l = 1$, $r_{cl} = 3$, and molecular mass $m_l = 1$ (the characteristic time $\tau_l = \sigma_l(m_l/\epsilon_l)^{1/2} = 1$). For the gas–liquid interaction, we adopt a modified LJ potential with the repulsive terms only, which takes $\sigma_{lg} = 1.2$, $\epsilon_{lg} = 0.5$ and $r_{c,lg} = 1.5$. As have been pointed out, these artificial values for inter-phase interaction are set deliberately to prevent the interpenetration of the two phases, so that the effect of phase-equilibrium can be excluded and the scale effect can be studied separately. Vaporization and condensation are theoretically still possible in this system, but actually the interpenetration between the two phases is rare.

Indeed, nano-gas bubbles are not easily observed in experiments, since usually strong Laplace pressure tends to crush them into the liquid phase. However, they do exist as reported by Gogotsi et al. (2001). Strong hydrophobic effect should present in this case, and therefore, the settings in our simulation should be relevant to real nano-bubbles, although the quantitative aspects are not comparable.

We have also tried different cut-off distances (1.2, 1.3, 1.5, and 3.0); they all present strong hydrophobicity on the phase-interface, but their effect on flow behavior was found to be not significant. The current value $r_{c,lg} = 1.5$ is chosen as a compromise between computational efficiency and numerical accuracy.

Although different cut-off distances and other parameters will result in different properties, which are not necessarily realistic, the nature of these properties and the flow behavior is still the same and can be described under the same theoretical framework of statistical mechanics

(kinetics) and hydrodynamics. That is, as long as the same set of similarity criteria is met, the molecular details, no matter realistic or fictitious, are not relevant to the flow behavior.

The solid walls in our channel flow simulations are represented by three layers of wall molecules which are located at the sites of a planar face-centered lattice with $\sigma_w = 1$ and $m_w = 1$. The pair interactions between wall molecules are identical to those between liquid molecules. Similar to Liem et al. (1992) and Xu and Zhou (2004), each wall molecule is assumed to be anchored at its lattice site by a Hooke spring with an additional harmonic potential of $\phi(s) = 1/2Cs^2$ (5)

where s is the displacement of the wall molecule from its lattice site, and the stiffness of the spring C is set to 75 for the relatively soft wall here. The strong interactions between wall- and fluid-molecules are represented by the truncated and shifted sixth-power soft sphere potential,

$$\phi(r_{ij}) = \begin{cases} 4\epsilon \left[\left(\frac{\sigma}{r}\right)^6 - \left(\frac{\sigma}{r_c}\right)^6 \right] & r_{ij} \leq r_c \\ 0 & r_{ij} > r_c \end{cases} \quad (6)$$

with $\sigma_{fw} = 1$, $r_{cfw} = 1$ and $\epsilon_{fw} = 0.875$.

2.2 Boundary conditions and thermostat

As shown in Fig. 1, the periodic boundary condition (PBC) is applied to our simulations wherever the flow domain is

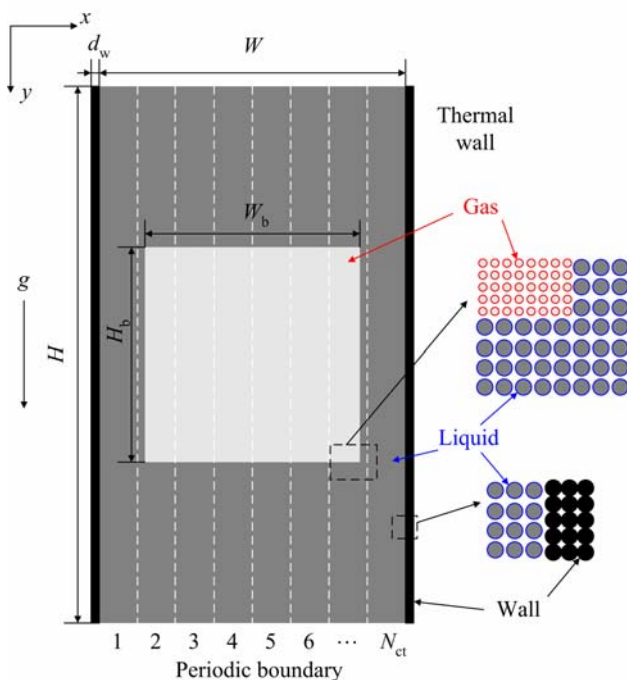


Fig. 1 Schematic diagram of the simulation setup for nano-channel flow

exposed to an unbounded environment in the flow direction. Therefore, the simulated system is effectively closed and any sustainable simulation has to provide a mechanism of heat removal, i.e., a thermostat, for which thermal walls are used in the simulations of channel flow. Applying more complicated thermostat to the flow field to maintain uniform temperature is not easy in such a tiny system with strong non-equilibrium flow. And on the other hand, with a thermostat on the bulk of the fluids, it would be difficult to study the shear heating effect in the system. Thermostat on the wall seems to interfere less to the physics of the system.

The temperature distribution in the simulated nano-channel flow is stabilized by rescaling the thermal velocity of the wall molecules per time step, i.e.,

$$\mathbf{V} = \left\langle \sum_{i \in \text{wall}} \mathbf{v}_i \right\rangle$$

$$v^2 = \left\langle \sum_{i \in \text{wall}} |\mathbf{v}_i - \bar{\mathbf{V}}|^2 \right\rangle \quad (7)$$

$$\mathbf{v}'_i = \frac{v_w}{v} (\mathbf{v}_i - \bar{\mathbf{V}})$$

In this way, a steady temperature gradient across the width of the channel develops eventually, along with a steady flow velocity profile, which enables a balanced transfer of viscous heat production to the cold walls where the temperature is kept constant at $k_B T_w = 1/2m_w v_w^2$.

2.3 Statistics and analysis

The motion of the particles is numerically tracked using the leap-frog algorithm (Frenkel and Smit 1996; Rapaport 2004). The interactions between soft particles are calculated first and then the collisions between the PPs are processed. To simplify the computation, reduced time steps are chosen as $\Delta t = 0.005$. Along with this dynamical evolution, non-intrusive “on-line measurements” are performed simultaneously by many passive procedures. They are various statistics and analysis on the results, which can be more convenient, efficient and memory economic than in the off-line mode, i.e., by employing a post-processor working on saved data.

In this work, the wall friction \mathbf{F}_w on the liquid is summed over the forces between liquid and wall particles; and the force \mathbf{F}_b on the bubble from the liquid is summed similarly. That is,

$$\mathbf{F}_w = \sum_{i \in \text{fluid}, j \in \text{wall}} \mathbf{f}_{ij} \quad (8)$$

$$\mathbf{F}_b = \sum_{i \in \text{gas}, j \in \text{liquid}} \mathbf{f}_{ij} \quad (9)$$

Similar to Xu and Zhou (2004), in the channel flow simulations shown in, the fluid area between two walls is

partitioned into N_{ct} (normally $N_{ct} = 30$) strips along the flow direction, and the width of each strip is then $\Delta x = W/N_{ct}$. We define the function

$$\delta_k(x_{i,t}) = \begin{cases} 1 & \text{if } (k-1)\Delta x < x_i < k\Delta x \\ 0 & \text{otherwise} \end{cases} \quad (10)$$

where the subscript t represents the current time. The number density in the k th strip from time t_1 to t_2 is then calculated by

$$n(k) = \frac{\sum_{t=t_1}^{t_2} \sum_{i=1}^N \delta_k(x_{i,t})}{H\Delta x(t_2 - t_1)} \quad (11)$$

where H is the height of the channel. The time interval for averaging $t_2 - t_1$ is typically 200 time units for fast flow to 1,000 time units for slow flow, which presents a compromise between statistical dispersion and dynamical resolution of the measurement. Consequently, the mean velocity in the strip, taken as the local flow velocity, is calculated as

$$u(k) = \frac{\sum_{t=t_1}^{t_2} \sum_{i=1}^N \delta_k(x_{i,t}) v_{i,t}^y}{(t_2 - t_1) \sum_{i=1}^N \delta_k(x_{i,t})} \quad (12)$$

and the local temperature is calculated as

$$k_B T(k) = \frac{\sum_{t=t_1}^{t_2} \sum_{i=1}^N \delta_k(x_{i,t}) m_i [v_{i,t}^z - u^z(k)]^2}{\text{dim} \cdot (t_2 - t_1) \sum_{i=1}^N \delta_k(x_{i,t})} \quad (13)$$

where $\text{dim} = 2$ in our cases, α represents x - and y -coordinates with $u^x(k) = 0$ and $u^y(k) = u(k)$.

At nano-scale, the properties of the fluids are usually different from those at macro-scales, depending on system size, boundary conditions, etc. Therefore, the values used in the present work are measured in the simulated systems directly, or in comparable systems of the same dimension, density and temperature. The pressure P is measured in equilibrium with (Allen and Tildesley 1989)

$$PV = Nk_B T + \frac{1}{\text{dim}} \sum_i \sum_{j>i} \mathbf{r}_{ij} \cdot \mathbf{F}_{ij} \quad (14)$$

In the following simulations, the gas composed of PP has an average packing fraction (η) about 0.15, which is well below its solidification limit, and therefore behaves like a normal compressible gas. Its compressibility factor can be related to η by $Z = 1/(1 - \eta)^2$. However, the pressure changes in our simulations were weak when compared to the absolute pressure of this gas, so the effect of compressibility is not significant in the process of bubble evolution.

As shown in Fig. 2, according to the Laplace law, when the bubble expand infinitesimally by ΔR , the incremental interfacial potential is $\Delta \Psi_s = 2\pi \Delta R \sigma$, and it is equal to the work by the pressure, $\Delta \Psi_s = (P_b - P_l) \cdot 2\pi R_b \Delta R$.

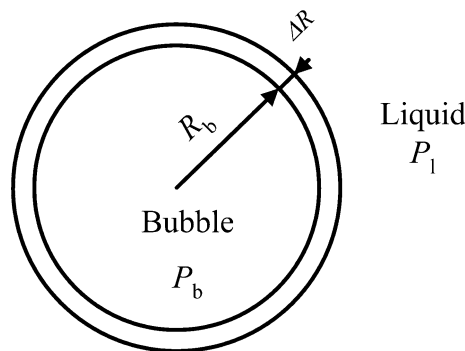


Fig. 2 Schematic diagram of a 2D circular gas bubble in liquid

Therefore, we calculate the interfacial tension for two-dimensional system as

$$\sigma = \Delta P \cdot R_b \quad (15)$$

where ΔP is the pressure difference between the two phases near the gas–liquid interface, $\Delta P = P_b - P_l$. Also, if the bubble shape is not circular, R_b in Eq. 4 represents the local curvature of the bubble and ΔP is the local pressure difference accordingly.

However, it is difficult to measure the gas–liquid interface area in molecular dynamics simulation; therefore, the “interfacial potential” ζ_s is summed over all pairs of gas–liquid interacting particles instead, that is,

$$\zeta_s = \sum_{i \in \text{gas}, j \in \text{liquid}} \phi_{ij} \quad (16)$$

Note that this potential may be not the actual interfacial free energy which is the product of interfacial tension (σ) and interfacial area, but the summed potential is considered to be approximately proportional to the interfacial area under certain density and temperature.

The shear viscosity μ can be calculated using a non-equilibrium molecular dynamics simulation [Poiseuille flow simulation in the channel usually, as in Xu et al. (2004) and Backer et al. (2005)] for Newtonian fluids with the equation

$$\mu = \tau / \frac{\partial u}{\partial x} \quad (17)$$

where τ is the shear stress, and $\frac{\partial u}{\partial x}$ is the shear rate.

2.4 Initial settings and properties of fluids

The simulated region is 120 by 200 with three-layer walls on both sides (the wall molecule number density $n_w = 1$ and total number $N_w = 1,200$). Initially, a rectangular gas bubble is placed at the center with the size 70 by 70 and number density $n_g = 1$. The gas particle number is $N_g = 4,900$. The liquid particles are placed around the gas bubble with the number density $n_l = 1/1.2^2 = 0.694$ and the

liquid particle number $N_l = 12,230$. Both gas and liquid particles are located at the sites of square lattices each corresponds to their number densities. Random initial velocities are set for gas, liquid and wall particles at a given temperature $T_0 = 0.45$.

It takes about 1,000 time units for the initial rectangular bubble to relax to the circular shape. In equilibrium, $n_l = 0.749$ (mass density $\rho_l = 0.749$) and $n_g = 0.758$ (mass density $\rho_g = 0.076$). Under these conditions, the liquid state of the LJ fluid is ensured from the phase diagram of the two-dimensional Lennard–Jones system (Barker et al. 1981) and then the corresponding properties are measured as $P_l = 0.163$, $\mu_l = 2.85$, $v_l = 3.80$, $P_g = 0.466$, $\mu_g = 0.158$, and $v_g = 2.09$. The bubble radius (R_b) thus measured, assuming circular shape, is 45.4 (gas volume 6.47×10^3), and the interfacial tension then calculated is $\sigma = 13.7$ using Eq. 4. Thereafter, a constant bulk force (gravity) is applied to drive the gas and liquid particles to flow. In most simulations, the gas bubble is considered to be almost uncompressed during its evolution, as confirmed by a visual measurement of the bubble volume, and the temperature of the fluids changes little. Thus, the properties gotten above are still valid for the cases with fluid flow.

The units of the characteristic quantities used for the reduced values in the present work are listed in Table 1.

3 Results and discussion

As an idealized model, we do not mean to simulate any specific gas or liquid in this study, but a general and reasonable one. We are mainly interested in the similarities or differences of gas–liquid flows at nano-scales to their macro-scale counterpart. For this purpose, we only need

our gas and liquid models to reproduce typical fluid flow behavior if they have enough numbers. Such flow behavior can be well characterized by similarity criteria such as Re and Ca , and therefore, the question which actual fluid our model presents is not so important for our purpose as long as we can get its material properties from simulations or statistical mechanics, and this can be ensured by our previous studies (Ge and Li 2003), existent literatures and basic principles of thermodynamics and statistical mechanics. That is, if an enormous system of such simple gas and liquid molecules are simulated, the macro-scale behavior of gas–liquid flow can surely be reproduced.

Of course, to compare its flow behavior with its macro-scale counterpart, we do impose some “extreme” conditions on this gas, for example, the super-hydrophobic phase interface to prevent the crushing of the bubble and the extremely high gravity (over 10^{10} times of normal gravity) to drive the fluid in nano-tube. Moreover, the mass and number density of the gas is much higher than normal macro-scale gas.

Under our simulation conditions, the absolute temperature variation in the system is not very large, so we have considered the mean viscosity of the LJ fluid only. This is obtained by carrying out duct flow simulations for the corresponding fluid under the corresponding mean temperatures and shear rates, just as in physical experiments.

3.1 Flow patterns in the nano-channel

Evolution of the flow patterns is the most obvious results we can get from these simulations and it is easily compared with macro-scale flows. The flow patterns found in the simulations of the gas–liquid flow in the nano-channel described earlier is reported in this subsection.

Table 1 Units of the characteristic quantities

Characteristic quantity	Unit		Value of argon atom	
	2D	3D	Reduced value	Dimensional value
Base quantity				
Mass, m	m_l	m_l	1	6.63×10^{-26} kg
Length, l	σ_l	σ_l	1	3.40×10^{-10} m
Energy, e	ε_l	ε_l	1	1.67×10^{-21} J
Temperature, T	ε_l/k_B	ε_l/k_B	1	120 K
Derived quantity				
Time, t	$\sigma_l(m_l/\varepsilon_l)^{1/2}$	$\sigma_l(m_l/\varepsilon_l)^{1/2}$	1	2.14×10^{-12} s
Velocity, u	$(\varepsilon_l/m_l)^{1/2}$	$(\varepsilon_l/m_l)^{1/2}$		
Number density, n	$1/\sigma_l^2$	$1/\sigma_l^3$		
Mass density, ρ	m_l/σ_l^2	m_l/σ_l^3		
Force, F	ε_l/σ_l	ε_l/σ_l		
Acceleration, a	$\varepsilon_l/(m_l\sigma_l)$	$\varepsilon_l/(m_l\sigma_l)$		
Pressure, P	ε_l/σ_l^2	ε_l/σ_l^3		
Viscosity, μ	$(\varepsilon_l m_l)^{1/2}/\sigma_l$	$(\varepsilon_l m_l)^{1/2}/\sigma_l^2$		

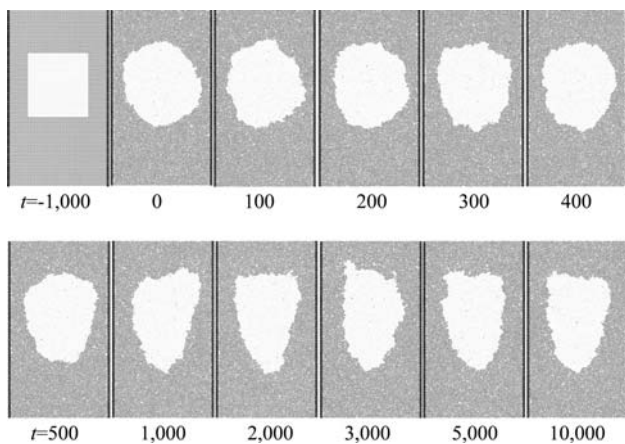


Fig. 3 Typical bubble motion and deformation in the nano-scale channel (at $g = 1 \times 10^{-3}$). To display the bubble integrally, the snapshots are taken on the mass center of the bubble

3.1.1 Temporal evolution of the flow pattern under given gravity

As shown in Fig. 3, the simulation begins with a rectangular bubble placed at the center of the channel ($t = -1,000$). The system is relaxed for 1,000 time units in the absence of gravity, during which the rectangular bubble deforms to a circular bubble under the action of interfacial tension and the interfacial energy reaches its minimum. Thereafter, both the gas and the liquid are accelerated by a constant bulk force of $g = 1 \times 10^{-3}$ and the bubble shape undergoes a series of changes until it stabilizes. Figure 4 represents the temporal variation of velocities, interfacial potential and corresponding forces.

As seen in Fig. 4, the considered variables reach saturation soon with little fluctuations. The stable wall friction on the fluids is equal to the total gravity force (the value is 12.72) and the drag force on the bubble also balances the gravity force on the bubble (the value is 0.49). The bubble undergoes significant deformation for a much longer time, as reflected by the increase and oscillation of interfacial potential. In this typical simulation, the bubble stabilizes at about 5,000 time units later.

The steady state is also reflected by the flow velocity and temperature profiles shown in Fig. 5 where the averaged values in each sampling strip containing both the gas and liquid phases are plotted, that is,

$$u_m = wu_{gas} + (1 - w)u_{liquid} \tag{18}$$

where w is the mass fraction of the gas phase defined as

$$w = m_{gas} / (m_{gas} + m_{liquid}) \tag{19}$$

and

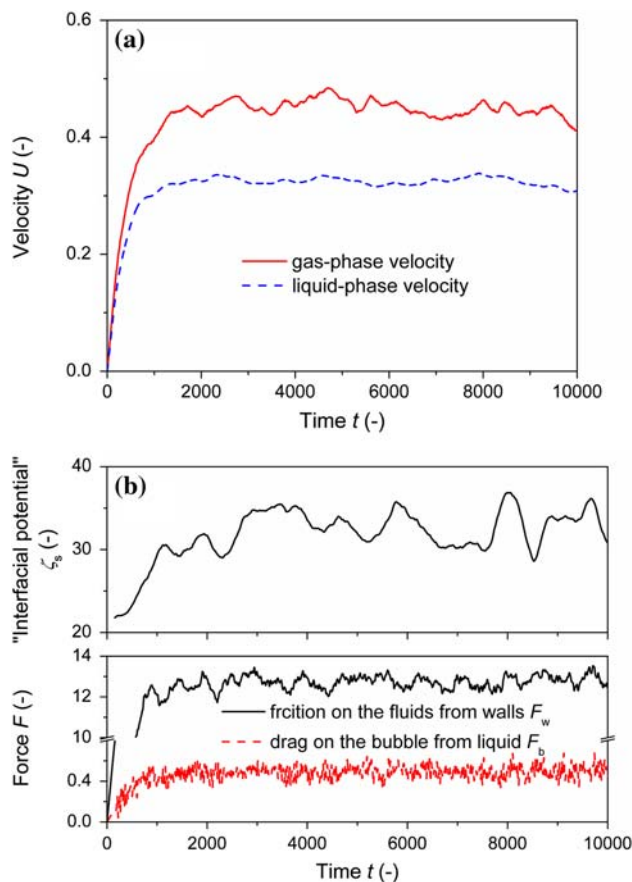


Fig. 4 Temporal variation at $g = 1 \times 10^{-3}$. **a** Velocities of the gas and liquid phases, **b** gas–liquid “interfacial” potential (upper panel) and forces (lower panel)

$$T_m = xT_{gas} + (1 - x)T_{liquid} \tag{20}$$

where x is the molar fraction of gas phase defined as

$$x = N_{gas} / (N_{gas} + N_{liquid}) \tag{21}$$

It can be noted that the profiles at $t = 5,000$ and $t = 10,000$ are virtually unchanged.

Limited by the heat-extracting ability of the constant temperature walls, the temperature of the fluid heated by strong shear friction is higher than the wall temperature as shown in Fig. 5. Although the fluid temperature is somewhere over the gas–liquid transition temperature for the two-dimensional LJ system and the LJ fluid is thus partially supercritical [the critical point constants are $T_c = 0.56$ and $n_c = 0.325$ according to Barker et al. (1981)], the LJ fluid under trans-critical conditions is more-like liquid in our case due to the existence of the attractive interaction with each other under the LJ potential.

The evolution of the bubble shape and the slug flow pattern found here is, to some extent, in accordance with its mini-scale counterparts as reported by Yang et al. (2002).

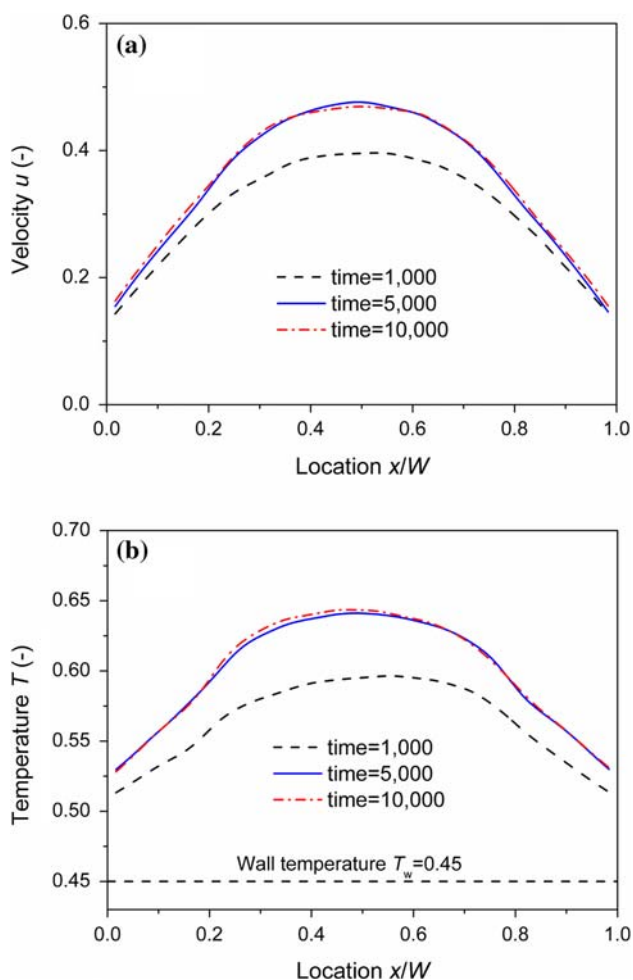


Fig. 5 Mass-averaged velocity profiles (a) and molar-averaged temperature profiles (b) in the nano-channel at different times at $g = 1 \times 10^{-3}$

The bubble typically composes of two parts, a rounded nose region in the front followed by a column section surrounded by an annular film of the liquid, although, in nano-flows, the bubble is in frequent fluctuation because of the significant thermal noise.

In fact, nano-gas bubbles are not easily observed in experiments, since usually strong Laplace pressure tends to crush them into the liquid phase. Real gas bubbles rather

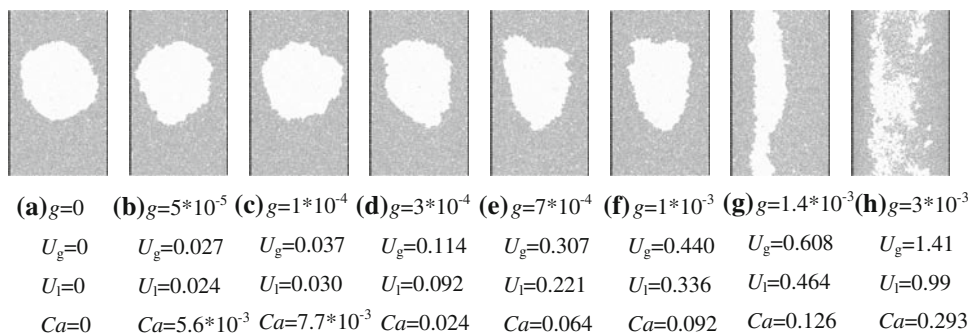
than cavities at nano-scales were indeed observed by Gogotsi et al. (2001) in a liquid-filled nano-tube with a diameter of about 50 nm. And in this case, strong hydrophobic effect should present to withstand this pressure. In previous three-dimensional simulations of nano-gas-liquid flows using soft potentials (Sushko and Cieplak 2001), the threshold gas molecule number for the existence of stable bubbles is about several hundred under similar conditions. In our two-dimensional molecular dynamics simulation, the bubble consists of 4,900 gas molecules (the bubble diameter is about $90\sigma_1$) and the interaction between two phases is tougher (with longer repulsion range); therefore, it seems reasonable to have stable nano-bubble in our case.

However, flow pattern presented here is quite different from the two-phase flow with cavity (Matsumoto and Matsuura 2004). The gas bubble constituting PPs moves hydrodynamically with a non-uniform velocity profile in the bubble; contrarily, MD-MD gas-liquid nano-flow suggests that the “nano-bubble” has the similar flow behavior as a nano-grain (Sushko and Cieplak 2001). We do not mean that our results are more realistic as compared to a specific physical system, but we want to demonstrate that, if such simple gas and liquid models are used, the results will like this, and therefore, if difference is observed in real experiments, the molecular details are more likely to be responsible for such difference.

3.1.2 Variation of the flow patterns with the intensity of gravity

In this work, various gravities ranging from 10^{-5} to 10^{-2} exert on the fluids to drive the flow in the nano-scale channel. As the mass density between the gas and liquid phases is not large, the gravity on the gas phase is, in fact, also a major driving force for the flowing of the mixture. But even though the gas phase is light as compared with the liquid phase, the force balance regarding the gas bubble is still that between bubble gravity and the drag force exerted (by the liquid phase) on the bubble. Because of the periodic boundary condition employed in our simulations, buoyancy does not take effect in this balance (Sushko and Cieplak 2001).

Fig. 6 Steady-state flow patterns under different intensities of gravity (typical snapshots). $Ca = \mu_l U_b / \sigma$ is the capillary number characterizing the gas-liquid flow pattern



Representative snapshots of the corresponding steady-state flow patterns are shown in Fig. 6. Four distinct flow regimes can be identified. Bubbly flow (Fig. 6b, c) is characterized by perfect or distorted (non-spherical) gas bubbles. With increasing gravity, the velocities of gas bubble and liquid film both increase, leading to slug flow (Fig. 6d–f) featuring an elongated gas segment composed of a rounded nose region and a column section, as described by Triplett et al. (1999). Under high gravity, and hence high velocities, the elongated segment in slug flow becomes unstable and ruptures finally and annular flow (Fig. 6g) establishes. When gravity is extremely high, the gas phase disperses in liquid phase as small bubbles by virtue of the strong shearing of the liquid, establishing the dispersed regime (Fig. 6h).

Surface tension and pressure have also significant impact on the systems we simulated, as reflected by the effect of the Ca number illustrated in Figs. 6 and 16. However, under the gravity range covered in our simulations, from 10^{-5} to 10^{-2} , the bubble volume changes little as compared to its equilibrium value without gravity as seen from the snapshots in Figs. 6a–f and 16a–c directly. The bubble pressure should, therefore, increase under higher gravity because of the increase in temperature due to shear heating. But we have not yet measured it directly.

The flow patterns reproduced so far are similar to the macro-scale counterpart, and are in good agreement with previous experiments in micro-channel (Kawaji and Chung 2004) and in mini-channel (Triplett et al. 1999). Although quantitative comparisons are still not possible owing to the strong thermal fluctuations that complicates the identification of flow patterns.

The stable temperature profile under various gravities (and hence various shear rates) takes a similar form. Lower temperature appears near the walls where heat is extracted by the thermostat while higher temperature appears inside the channel due to accumulated shear heating, as shown in Fig. 7b. Interestingly, the highest temperature does not appear at the center of the channel but at inside the gas bubble indicated by the much lower mass-averaged density in Fig. 7a. It reflects weaker heat transfer in the gas phase as compared to the liquid phase. The variation of temperature over the pipe affects the material properties and hence the gas–liquid flow behavior. But in the following discussions, averaged properties are used. For the liquid phase, the temperature range observed in our simulations is from 0.45 to 0.70 with certain statistical error, and the corresponding viscosity range is from 4.0 to 3.5. For the gas phase, the temperature difference is even smaller. Therefore, the increase of bubble pressure by shear heating is neglected as compared to the absolute bubble pressure.

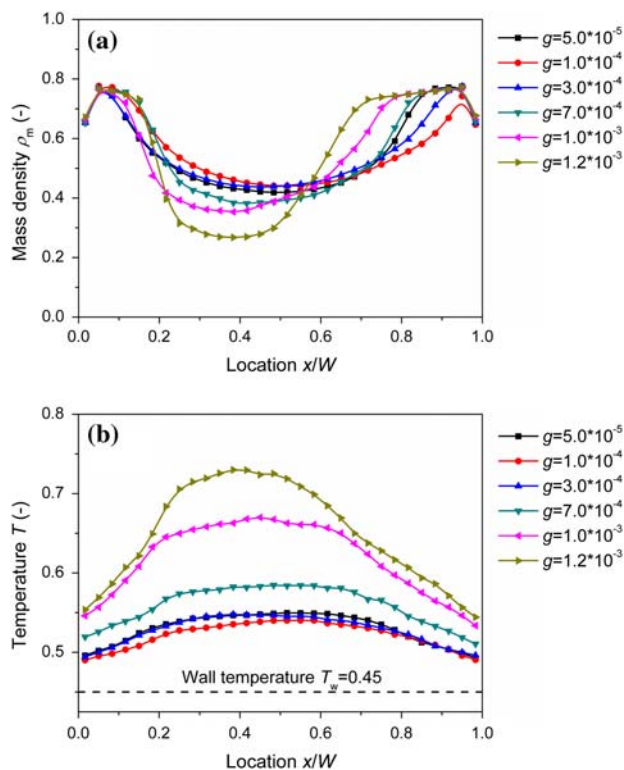


Fig. 7 Steady mass-averaged density profiles (a) and molar-averaged temperature profiles (b) under different intensities of gravity

3.2 Bubble terminal velocity and slippage at the wall

In this subsection, we try to understand the simulated gas–liquid nano-flow quantitatively. The terminal velocity of the gas bubble is compared with macro-scale hydrodynamic results, and the slippage at the wall is analyzed with the obtained velocity profiles.

3.2.1 Terminal velocity of the bubble

The drag force on a spherical droplet or bubble driven by gravity in infinite static fluid is given by Landau and Lifshitz (1987) as

$$F_D = 2\pi R\mu \frac{2\mu + 3\mu'}{\mu + \mu'} U \tag{22}$$

where μ and μ' are the viscosities of the surrounding fluid and the moving fluid object, respectively. And the drag coefficient C_D is then calculated as

$$C_D = \frac{F_D}{\pi R^2 \cdot \rho U^2 / 2} = \frac{4\pi\mu}{U\rho R} \frac{2\mu + 3\mu'}{\mu + \mu'} = \frac{8}{Re} \frac{2\mu + 3\mu'}{\mu + \mu'} \tag{23}$$

where the Reynolds number is defined as $Re = 2RU\rho/\mu$. Assuming that this C_D also holds for two-dimensional

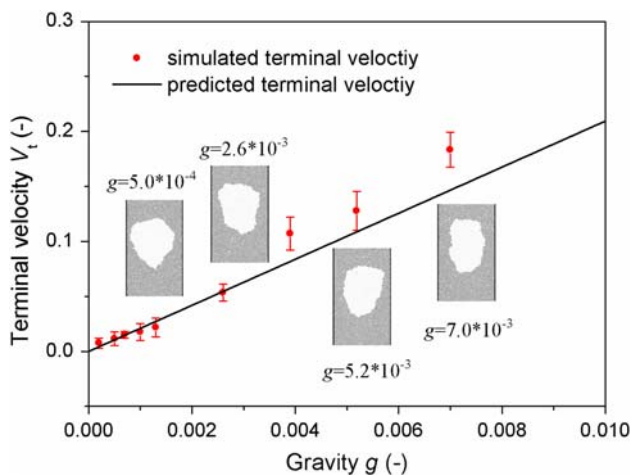


Fig. 8 Terminal bubble velocity for the cases with gravity exerted on the bubble only. The line represents hydrodynamic prediction from Eq. 14 and the scattered points with standard deviation error bars present the simulation results

moving objects between the confining walls,¹ the drag force is then

$$F_D = C_D \cdot A_p \cdot \rho U^2 / 2 = 4\mu \frac{2\mu + 3\mu'}{\mu + \mu'} U \tag{24}$$

where A_p is the projected area of the moving object in the flow direction. For two-dimensional column-like moving object in this work, $A_p = 2R$. The terminal speed V_t is then determined by the balance between the gravity force on the moving object G_b and the drag force, that is,

$$V_t = \frac{G_b(\mu + \mu')}{4\mu(2\mu + 3\mu')} \tag{25}$$

Note that with the imposition of periodic boundary conditions in the axial direction, the buoyancy is considered not present in the simulations.

Note that, 2D simulation is meaningful only in terms of hydrodynamics. 2D molecule does not exist in reality, but in statistical mechanics gas composed of 2D molecules do have 2D material properties (with different dimensionality to 3D properties). For two-dimensional flow, such as the perpendicular flow past an infinitely long cylinder, the same formulation should hold for both purely 2D fluid or 3D fluid in 2D flow (hydrodynamic instability along the cylinder axis should not be considered at this stage), the difference is that 2D or 3D material properties should be used, respectively, and this is the case of Eqs. 23–25. In

¹ We have found no general drag coefficient for two-dimensional deformable moving object thus far, and we understand that, according to Huang and Feng (1995) and Chakraborty et al. (2004), the drag force on cylinder is also strongly influenced by the presence of confining walls; but, the drag coefficient for sphere consists with the circular cylinder to an acceptable accuracy in the Reynolds number range of 10^0 to 10^1 . Therefore, this C_D is used as a rough estimate.

particular, Eq. 24 holds for both 2D fluid and 3D fluid in 2D flow, but for 3D fluid in reality, we should use normal 3D viscosity and the projected area has the dimension of “length²”, while for 2D fluid we have used 2D viscosity and the projected “area” actually has the dimension of “length” only.

We now consider the case in which the gravity is applied only to the moving object to simulate the gravity-driven sedimentation in a two-dimensional channel. And the simulating results are represented in Fig. 8. It is found that the hydrodynamic prediction from Eq. 14 yields quite consistent terminal velocity with the simulating results. The departure may be ascribed to the perturbing effects from the walls and the deviation from the circular shape of the gas bubble. It is also found that, when gravity is very high, the variation of liquid density around the bubble can no longer be ignored, and hence the simulation results deviate from the prediction of Eq. 14.

This qualitative agreement of the hydrodynamic prediction for gas–liquid two-phase flows in channels about 40 nm ($114\sigma_1$) echoes the findings of Travis et al. (1997) in molecular dynamics simulation of three-dimensional single-phase channel flow, while the channel width equals $10.2\sigma_1$, where the solution of the Navier–Stokes equations also holds basically. Now, the applicability of the hydrodynamic description is extended to nano-scale two-phase flows.

3.2.2 Velocity profiles of channel flows

In our simulation, as shown in Fig. 9, the velocity profile for the bubble in the center is also parabolic-like, suggesting that the bubble gotten by our coupled method is moving hydrodynamically. This is different from the

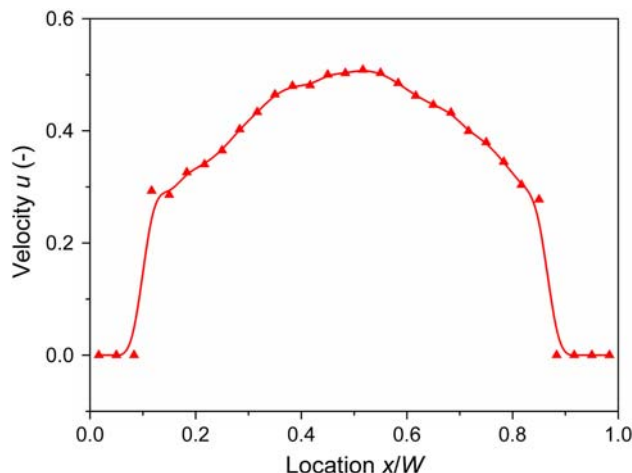


Fig. 9 Velocity profile for the bubble at $g = 1 \times 10^{-3}$. The bubble is almost located at the center of the channel in our simulation

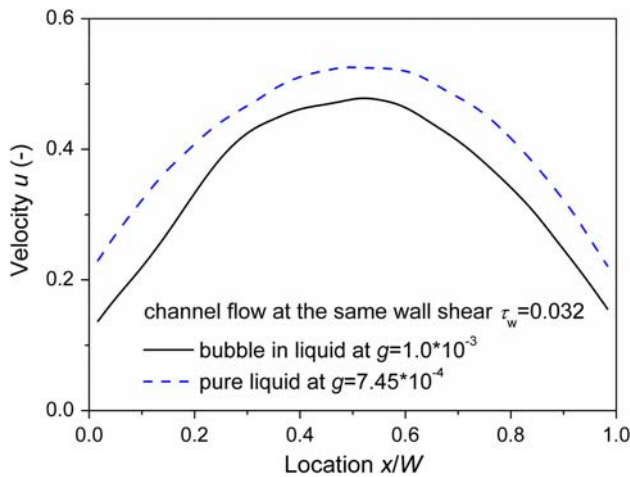


Fig. 10 Velocity profiles of two-phase flow and single-phase flow at the same wall shear stress $\tau_w = 0.032$. Here the velocity in two-phase flow is mass-averaged with Eq. 7

LJ-type “gas bubble” in the previous study (Sushko and Cieplak 2001), which is said to behave like a frozen solid object, having a homogeneous falling velocity that is about ten times larger than the hydrodynamic prediction.

We also compare the velocity profiles of two-phase flow with corresponding pure liquid flow at the same wall shear stress ($\tau_w = 0.032$), shown in Fig. 10. It is seen that the wall slip velocity of pure liquid flow is much higher, and the velocity profile of two-phase flow is a little bit flatter in the region containing the bubble, which is almost at the center of the channel. Therefore, it may be said that the presence of the gas bubble has changed the slip behavior of the LJ fluid on solid walls in our case, although the gas bubble does not interact with the walls directly. As far as we know it is not reported previously, and the details are still in studying.

Due to the difference of the kinematic viscosities involved, the velocity profiles determined in the strips containing both gas particles and liquid particles depart from the quadratic form for Poiseuille-like flow (see the mid parts of the curves in Figs. 10 and 11, where the asymmetrical velocity profiles are caused by the biased bubble in the annular flow in the nano-channel).

However, for low-gravity cases ($g < 1 \times 10^{-3}$), neglecting the strips containing both gas and liquid, the velocities of gas–liquid two-phase flow in the strips away from the bubble do accord with quadratic velocity profile of Poiseuille flow well, as their counterparts of pure liquid flow, shown in Fig. 12. In fact, the quadratic curves can also be derived from hydrodynamic prediction using known flow parameters.

It should be emphasized that the quadratic form is valid only for relatively low-gravity cases, but not suitable for higher gravity cases. Under low gravity, the bubble is

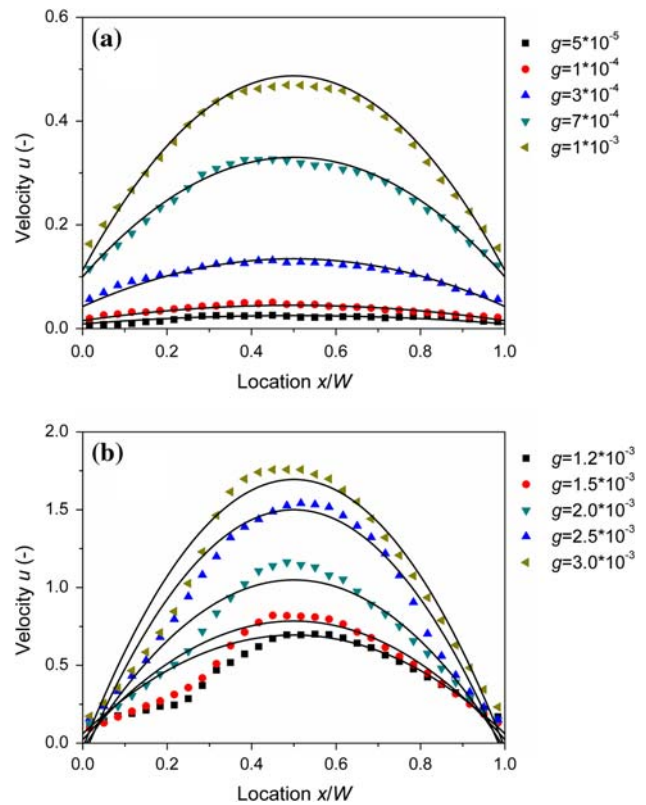


Fig. 11 Steady-state mass-averaged velocity profiles of gas–liquid two-phase Poiseuille-like flows in the channel under different gravitational accelerations, (a) low-gravity cases and (b) high-gravity cases. The scattered points represent the mean velocity profiles obtained from simulations and the lines represent the corresponding quadratic velocity profiles for Poiseuille flows

statistically symmetric and located almost at the center of the channel; hence the shears on the two sidewalls and on the gas–liquid interface could be considered equal, which lead to the quadratic velocity profile in the annulus area only occupied by the liquid phase. Note that this is a time-averaged profile. For the transient flow field, the presence of the gas bubble will certainly affect the liquid phase flow velocities around it. Under higher gravities, the gas bubble moves more and more dynamically and is prone to be located asymmetrically about the center of the channel, and therefore, the quadratic form is no longer valid.

3.2.3 Slippage at the wall

Slippage at walls is characteristic of nano- and micro-scale flows; this can be seen in both Fig. 12a and b where the velocity slippage increases with increasing gravity and hence increasing wall shear rate. This slippage can be described by the slip length (L_s), defined as how far the fluid should travel beyond the solid wall to reach the same velocity as the wall surface. L_s is usually calculated using the Navier hypothesis (Lamb 1932) as

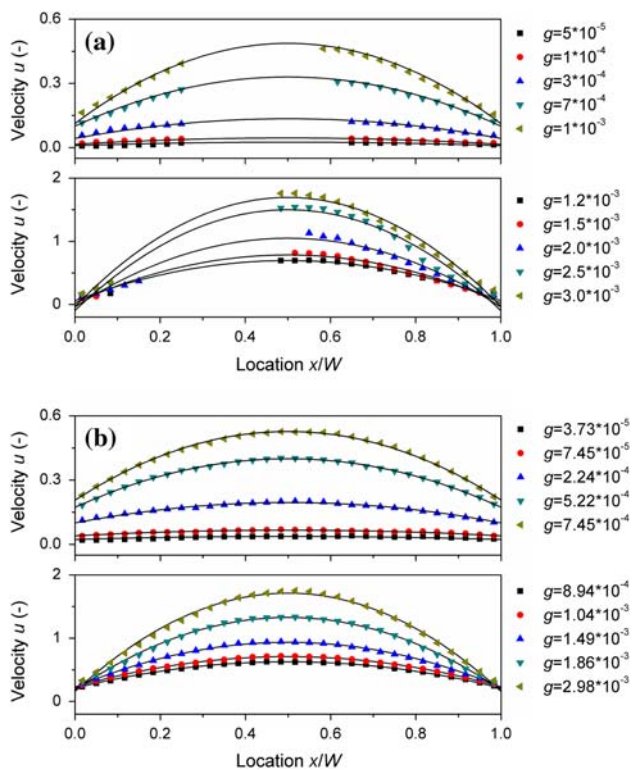


Fig. 12 Velocity profiles of (a) gas–liquid two-phase flows neglecting velocities in the strips containing both gas and liquid particles and of (b) pure liquid flows in the channel under different gravity, the upper row for the low g part and the lower row for the high g part

$$L_s = U_{\text{wall}} / \dot{\gamma}_{\text{wall}} \tag{26}$$

where L_s denotes the slip length, U_{wall} is the velocity difference between the wall and adjacent liquid, $U_{\text{wall}} = U_{\text{slip}}$, and $\dot{\gamma}_{\text{wall}} = \left. \frac{du(x)}{dx} \right|_{\text{wall}}$ is the shear rate at the wall. The slip behavior depends on fluid parameters as well as surface roughness, wettability, shear rate, etc.

The velocity profile of Poiseuille flow with slippage at walls is expressed by a quadratic function as

$$u(x/W) = 4(U_{\text{max}} - U_{\text{slip}})(x/W)(1 - x/W) + U_{\text{slip}} \tag{27}$$

where x is the lateral location, U_{max} is the maximum velocity that appears at the center line of the channel and U_{slip} denotes the slip velocity at walls. The shear rate at the wall is thus calculated as

$$\dot{\gamma}_{\text{wall}} = \left. \frac{du(x)}{dx} \right|_{\text{wall}} = 4(U_{\text{max}} - U_{\text{slip}})/W \tag{28}$$

and the slip length can be calculated as

$$L_s = \frac{U_{\text{slip}}}{4(U_{\text{max}} - U_{\text{slip}})} W \tag{29}$$

The slip velocity and slip length for both gas–liquid two-phase flow and pure liquid flow under variant shear stress

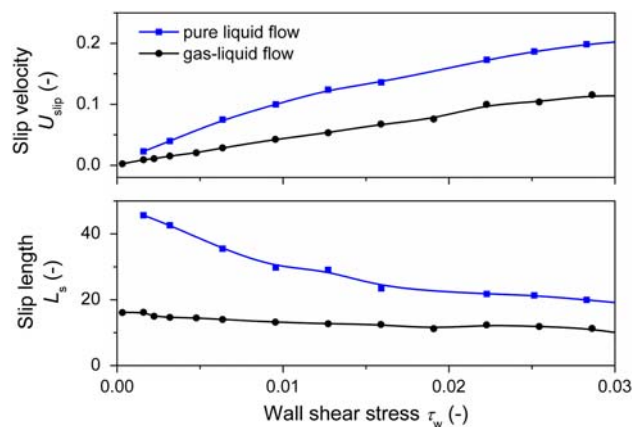


Fig. 13 Slip velocity (upper panel) and slip length (lower panel) versus wall shear stress

are shown in Fig. 13. For both pure liquid flow and gas–liquid flow, the slip lengths decrease almost linearly with increasing wall shear stress first, and then decrease slowly to a platform. The trend is similar to some previous studies (Xu and Zhou 2004), but different wall conditions and dimensions result in large quantitative difference. Moreover, the presence of gas bubble seems to reform the structure of the surrounding liquid and hence influences fluid–solid interaction indirectly. Under the same wall condition, the slippage of liquid on walls in two-phase flow is much weaker than that in pure liquid flow in the low wall shear stress region. And the variation of the slip length versus wall shear stress for two-phase flow is much flatter as shown in the lower panel of Fig. 13.

Note that, the slippage is only considered for the low-gravity cases as a rough estimate for the qualitative tendencies of slip length on its major dependent values. Due to the inaccuracy of the quadratic function in the high-gravity cases, the slippage is not characterized for these cases, and it is subject to future work.

On the other hand, the slip behavior is also strongly influenced by the wall configuration and liquid–wall interaction. In the present work, because of the simplified wall condition and molecular models used, the slip velocity is obviously seen at the liquid–solid boundary in the velocity profiles. This can be understood as a scale-effect of this idealized system, and on the other hand, as an indication that the no slip boundary condition is not intrinsic to hydrodynamics but depends on microscopic properties. It will be a very interesting topic for further study how wall configuration affects slippage.

3.3 Elementary three-dimensional simulations

So far, we have carried out 2D simulations only. Although many 2D gas–liquid simulations and experiments (in

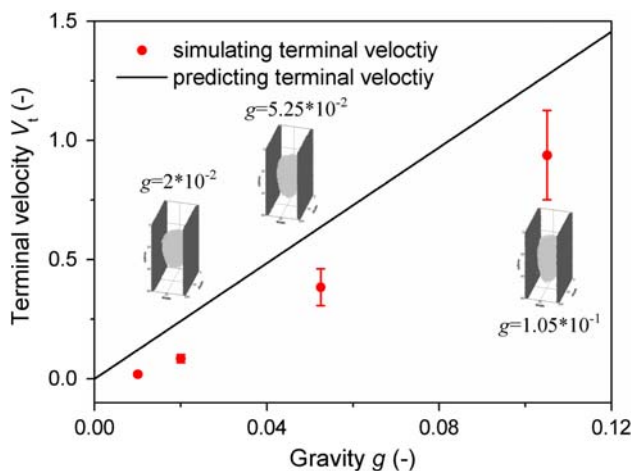


Fig. 14 Terminal bubble velocity in three-dimensional system. Gravity is exerted on the bubble only. The line represents hydrodynamic prediction from Eq. 11 and the scattered points with standard deviation error bars present the simulation results

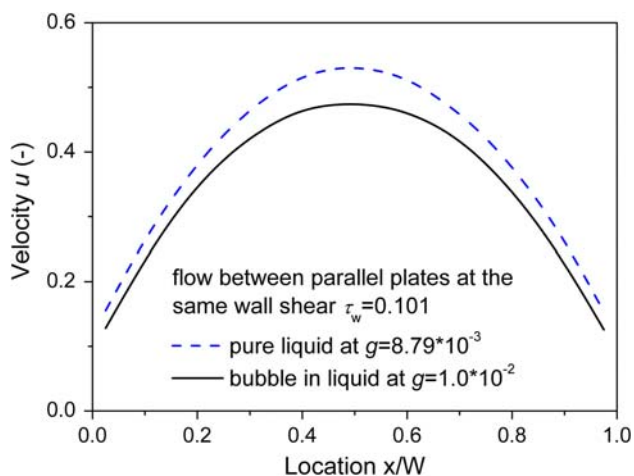
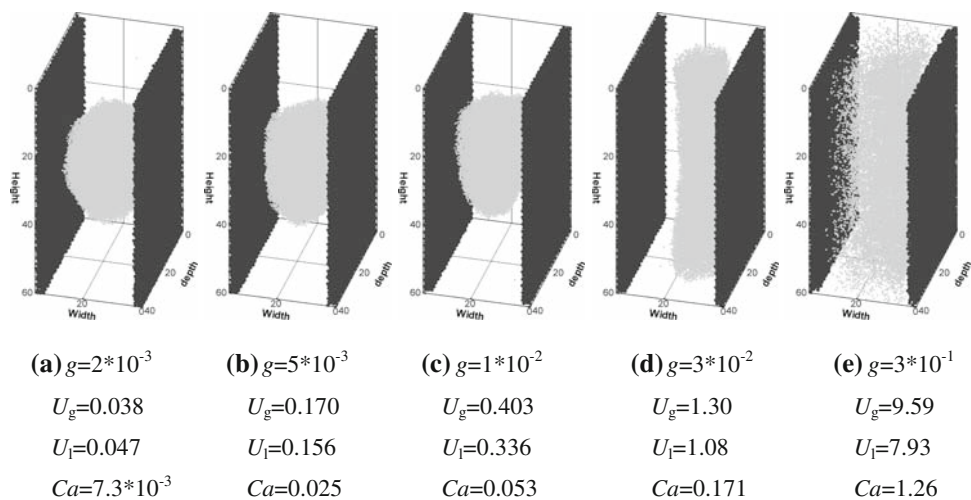


Fig. 15 Velocity profiles of three-dimensional two-phase flow and single-phase flow at the same wall shear stress $\tau_w = 0.101$ between parallel plates

Fig. 16 Steady-state flow patterns under different intensities of gravity between parallel plates (only wall particles and gas particles are shown in typical snapshots). $Ca = \mu_l U_b / \sigma$ is the capillary number characterizing the gas-liquid flow pattern. **a** Bubbly flow, **b** slug flow, **c** annular flow, **d** dispersed flow



pseudo-2D systems between narrow slots) have been reported (e.g., Yang et al. 2002 and so on) and they can be visualized and compared easily, it is still necessary to validate the results obtained in 2D simulations in physically “realistic” systems. For this purpose, we also apply this coupled method to 3D gas–liquid flows at nano-scale. The simulated region is set 36 by 60 in the planar direction and 40 in depth with three-layer parallel plates (wall molecules number $N_w = 14,400$), and the fluid space ($30 \times 60 \times 40$) contains 23,125 gas molecules with $m_g = 0.2$ and 43,925 liquid molecules with $m_l = 1$. The plate temperature is kept at $T = 1$ using direct velocity rescaling for wall molecules. The bubble is cuboid at the beginning and relaxed to a (nearly) spherical one with its radius $R_b = 15.2$ in the absence of gravity. The given gravity is then applied to the system and drives the fluids to flow. The material properties measured are $P_l = 0.832$, $\mu_l = 1.82$, $v_l = 2.37$, $P_g = 2.35$, $\mu_g = 0.43$, and $v_g = 1.37$. Therefore, the interfacial tension (for three-dimensional system) $\sigma = \Delta P \cdot R_b / 2 = 11.5$.

As shown in Fig. 14, under different gravities, the terminal velocities measured in the simulation are of the same order as predicted by Eq. 11 for 3D bubbles in infinite fluid. The over-prediction of Eq. 11 may again be ascribed to the additional resistance from the confining plates (Huang and Feng 1995; Chakraborty et al. 2004). The comparison of the velocity profiles of two-phase flow with corresponding pure liquid flow at the same wall shear stress ($\tau_w = 0.101$) is represented in Fig. 15. Similar to two-dimensional cases, the slip velocity of liquid on solid in pure liquid flow is higher than that in gas–liquid two-phase between parallel plates. And as expected, the evolution of bubble deformation is similar to two-dimensional case, and the flow patterns are also consistent with their macro-scale counterpart, as shown in Fig. 16.

4 Conclusions

In this paper, pseudo-particle modeling (PPM) is coupled with molecular dynamics simulation to investigate gas–liquid two-phase flow at nano-scale. By virtue of this approach, a clear and sharp interface between gas phase and liquid phase can be kept through only the interactions between gas and liquid molecules, without any artificial constraints.

In the present work, we investigate the flow pattern and slippage at wall for gas–liquid two-phase nano-channel flow with our coupled molecular dynamics method. Despite quantitative differences, our simulating results at nano-scale (much less than 1 μm) and under extremely high gravity (10^{10} times over normal gravity) agree in general with previous experiments and CFD simulations at micro- and macro-scale. Of course, the simulation also shows unique features of this distinct gas–liquid flow. Namely, parabolic velocity profile for the gas bubble is obtained in our simulation, while non-hydrodynamic behavior is found for LJ-type gas bubble (Sushko and Cieplak 2001). We also found that the gas bubble has significant influence on the slip behavior of the liquid on walls for two-phase channel flow although the gas and the wall do not interact with each other directly.

Acknowledgments This work was financially supported by the National Natural Science Foundation of China under the grant nos. 20336040, 20490201 and 20221603, and the Chinese Academy of Sciences under the grant KJCX-SW-L08.

References

- Allen MP, Tildesley DJ (1989) Computer simulation of liquids. Oxford University Press, New York
- Backer JA, Lowe CP, Hoefsloot HCJ, Iedema PD (2005) Poiseuille flow to measure the viscosity of particle model fluids. *J Chem Phys* 122(15):154503–154506
- Barker JA, Henderson D, Abraham FF (1981) Phase diagram of the two-dimensional Lennard–Jones system: evidence for first-order transitions. *Phys A Stat Theor Phys* 106(1, 2):226–238
- Chakraborty J, Verma N, Chhabra RP (2004) Wall effects in flow past a circular cylinder in a plane channel: a numerical study. *Chem Eng Process* 43(12):1529–1537
- Chobana ER, Markoski LJ, Wieckowski A, Kenis PJA (2004) Microfluidic fuel cell based on laminar flow. *J Power Sources* 128:54–60
- Denniston C, Robbins MO (2001) Molecular and continuum boundary conditions for a Miscible binary fluid. *Phys Rev Lett* 87(17):178302
- Ellisab JS, Thompson M (2004) Slip and coupling phenomena at the liquid–solid interface. *Phys Chem Chem Phys* 6:4928–4938
- Frenkel D, Smit B (1996) Understanding molecular simulation: from algorithms to applications. Academic Press, Orlando
- Gad-el-Hak M (1999) The fluid mechanics of microdevices—the freeman scholar lecture. *J Fluids Eng* 121:5–33
- Gad-el-Hak M (2005) Liquids: the holy grail of microfluidic modeling. *Phys Fluids* 17:100612
- Ge W (1998) Multi-scale simulation of Fluidization. Heat Energy Engineering, Harbin Institute of Technology, Ph.D., 125
- Ge W, Li J (2003) Macro-scale phenomena reproduced in microscopic systems: pseudo-particle modeling of fluidization. *Chem Eng Sci* 58(8):1565–1585
- Ge W, Ma J, Zhang J, Tang D, Chen F, Wang X, Guo L, Li J (2005) Particles methods for multi-scale simulation of complex flows. *Chin Sci Bull* 50(11):1057–1069
- Gogotsi Y, Libera JA, Guvenc-Yazicioglu A, Megaridis CM (2001) In situ multiphase fluid experiments in hydrothermal carbon nanotubes. *Appl Phys Lett* 79(7):1021–1023
- Gogotsi Y, Naguib N, Libera JA (2002) In situ chemical experiments in carbon nanotubes. *Chem Phys Lett* 365:354–360
- Hannon L, Lie GC, Clementi E (1986) Molecular dynamics simulation of channel flow. *Phys Lett A* 119(4):174–177
- Ho C-M, Tai Y-C (1998) Micro-electro-mechanical-systems (MEMS) and fluid flows. *Annu Rev Fluid Mech* 30:579–612
- Huang PY, Feng J (1995) Wall effects on the flow of viscoelastic fluids around a circular cylinder. *J Non-Newtonian Fluid Mech* 60(2):179–198
- Jensen KF (1999) Microchemical systems: status, challenges, and opportunities. *AIChE J* 45(10):2051–2054
- Kawaji M, Chung PM-Y (2004) Adiabatic gas–liquid flow in microchannels. *Microscale Thermophys Eng* 8:239–257
- Kotsalis EM, Walther JH, Koumoutsakos P (2004) Multiphase water flow inside carbon nanotubes. *Int J Multiphase Flow* 30:995–1010
- Lamb H (1932) Hydrodynamics. Dover, New York
- Landau LD, Lifshitz EM (1987) Fluid Mechanics. Pergamon Press, Oxford
- Liem SY, Brown D, Clarke JHR (1992) Investigation of the homogeneous-shear nonequilibrium-molecular-dynamics method. *Phys Rev A* 45(6):3706–3713
- Marin M, Risso D, Cordero P (1993) Efficient algorithms for many-body hard particle molecular dynamics. *J Comput Phys* 109:306–317
- Matsumoto M, Matsuura T (2004) Molecular dynamics simulation of a rising bubble. *Mol Simul* 30(13–15):853–859
- Peters GH, Eggebrecht J (1995) Observation of droplet growth and coalescence in phase-separating Lennard–Jones fluids. *J Phys Chem* 99(32):12335–12340
- Rapaport DC (2004) The art of molecular dynamics simulation. Cambridge University Press, Cambridge
- Stone HA, Stroock AD, Ajdari A (2004) Engineering flows in small devices: microfluidics toward a lab-on-a-chip. *Annu Rev Fluid Mech* 36:381–411
- Sun M, Ebner C (1992) Molecular-dynamics simulation of compressible fluid flow in two-dimensional channels. *Phys Rev A* 46(8):4813–4819
- Sushko N, Cieplak M (2001) Motion of grains, droplets, and bubbles in fluid-filled nanopores. *Phys Rev E* 64(21):021061–021008
- Thompson PA, Troia SM (1997) A general boundary condition for liquid flow at solid surfaces. *Nature* 389:360–362
- Travis KP, Todd BD, Evans DJ (1997) Departure from Navier–Stokes hydrodynamics in confined liquids. *Phys Rev E* 55(4):4288–4295
- Triplett KA, Ghiaasiaan SM, Abdel-Khalik SI, Sadowski DL (1999) Gas–liquid two-phase flow in microchannels Part I: two-phase flow patterns. *Int J Multiph Flow* 25(3):377–394
- Wang L, Ge W, Chen F (2007) Pseudo-particle modeling for gas flow in microchannels. *Chin Sci Bull* 52(4):450–455
- Xu JL, Zhou ZQ (2004) Molecular dynamics simulation of liquid argon flow at platinum surfaces. *Heat Mass Transf* 40:859–869
- Xu JL, Zhou ZQ, Xu XD (2004) Molecular dynamics simulation of micro-Poiseuille flow for liquid argon in nanoscale. *Int J Numer Methods Heat Fluid Flow* 14(5/6):664–688

Yang ZL, Palm B, Sehgal BR (2002) Numerical simulation of bubbly two-phase flow in a narrow channel. *Int J Heat Mass Transf* 45:631–639

Yarin AL, Yazicioglu AG, Megaridisb CM (2005) Theoretical and experimental investigation of aqueous liquids contained in carbon nanotubes. *J Appl Phys* 97:124309–124313